Scalable hyperfine qubit state detection via electron shelving in the $^2D_{5/2}$ and $^2F_{7/2}$ manifolds in $^{171}Yb^+$

C. L. Edmunds,[1,*] T. R. Tan,[1] A. R. Milne,[1] A. Singh,[1,†] M. J. Biercuk,[1,2] and C. Hempel[1,3,‡]

[1]*ARC Centre of Excellence for Engineered Quantum Systems, School of Physics, University of Sydney, Sydney, New South Wales 2006, Australia*

[2]*Q-CTRL Pty Ltd, Sydney, New South Wales 2006, Australia*

[3]*The University of Sydney Nano Institute (Sydney Nano), University of Sydney, Sydney, New South Wales 2006, Australia*

(Received 29 December 2020; accepted 9 June 2021; published 19 July 2021)

Qubits encoded in hyperfine states of trapped ions are ideal for quantum computation given their long lifetimes and low sensitivity to magnetic fields, yet they suffer from off-resonant scattering during detection, often limiting their measurement fidelity. In $^{171}Yb^+$ this is exacerbated by a low fluorescence yield, which leads to a need for complex and expensive hardware, a problematic bottleneck especially when scaling up the number of qubits. We demonstrate a detection routine based on electron shelving to address this issue in $^{171}Yb^+$ and achieve a 5.6× reduction in single-ion detection error on an avalanche photodiode to $1.8(2) \times 10^{-3}$ in a 100 μs detection period and a 4.3× error reduction on an electron multiplying CCD camera with $7.7(2) \times 10^{-3}$ error in 400 μs. We further improve the characterization of a repump transition at 760 nm to enable a more rapid reset of the auxiliary $^2F_{7/2}$ states populated after shelving. Finally, we examine the detection fidelity limit using the long-lived $^2F_{7/2}$ state, achieving further 300× and 12× reductions in error to $6(7) \times 10^{-6}$ and $6.3(3) \times 10^{-4}$ in 1 ms on the respective detectors. While shelving-rate limited in our setup, we suggest various techniques to realize this detection method at speeds compatible with quantum information processing, providing a pathway to ultrahigh-fidelity detection in $^{171}Yb^+$.

DOI: 10.1103/PhysRevA.104.012606

I. INTRODUCTION

Trapped ions have seen a resurgence as a leading platform for the development of quantum information systems. In recent years, a primary area of research has been the quality of single- and two-qubit gates, where fidelities of better than 99.999% [1,2] and 99.9% [3,4] have been reported, respectively. Enabled by quantum control techniques, such as amplitude, frequency, and phase modulation [5–7], high-fidelity two-qubit gates are now possible at high speeds [8,9] and also across larger qubit registers [10,11]. Progress in this domain has allowed for the implementation of longer and more complex quantum circuits (e.g., [12–14]). Yet, as the number of qubits in a joint register, and thereby the potential size of a correlated state, grows, an increasingly important area for improvement becomes state-detection fidelity. Detection errors are generally statistically independent and scale at least linearly with the number of qubits. They therefore quickly become a significant factor limiting the overall performance of a multiqubit register, e.g., in the context of active quantum error correction conditioned on stabilizer measurements [14–17].

Various qubit encodings are available in trapped ions which bring with them different advantages and drawbacks, including in the area of demonstrated measurement fidelity. One can either choose two ground states of the fine or hyperfine structure for the encoding or split the logical states across a ground and a metastable state to form an optical qubit [18]. Hyperfine qubits such as $^9Be^+$ [3], $^{43}Ca^+$ [19,20], and $^{171}Yb^+$ [21], as considered here, are an attractive choice in that they do not suffer from energy relaxation (T_1 decay) like optical qubits and also offer so-called clock states that are first-order insensitive to perturbations from magnetic fields (providing long T_2 coherence). Here the qubit states are separated by microwave frequencies on the order of several to tens of gigahertz, enabling the use of low-noise microwave sources for high-fidelity qubit control [1,22,23].

Measurement on either category of trapped-ion qubit is generally performed using state-dependent laser-induced fluorescence [24], whereby one logical state, the bright state, scatters photons and the other does not, hence being referred to as the dark state. Optical qubits enable efficient discrimination between these states and have shown high detection fidelities, leveraging the large energy-level separation of the qubit manifold [25,26]. By contrast, when using hyperfine qubits the relatively small energy gap between the qubit states results in unwanted off-resonant scattering during detection. This scattering limits the useful duration of the detection period and thereby the number of photons that can be collected in it, negatively impacting the ability to distinguish qubit states from associated photon-detection-probability distributions. To overcome this obstacle, one may pursue the

*Present address: Institute for Experimental Physics, University of Innsbruck, Innsbruck 6020, Austria; edmunds.claire@gmail.com

†Present address: Department of Physics, University of California, Berkeley, California 94720, USA.

‡Present address: Paul Scherrer Institut, Villigen PSI 5232, Switzerland; cornelius.hempel@gmail.com

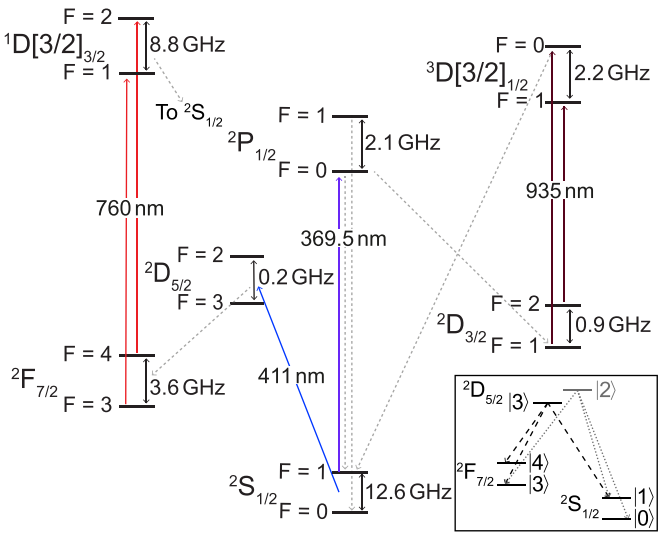

FIG. 1. Selected energy levels and laser frequencies for ^{171}Yb$^+$. The qubit levels are encoded in the $^2S_{1/2}$ hyperfine manifold, shown at the bottom center. Zeeman levels have been omitted for visual clarity and the dashed gray lines show relevant spontaneous decays. The inset shows decay channels from $^2D_{5/2}$, with simplified hyperfine notation.

use of new complex imaging and detection hardware [27–31] or software-based data processing of time-resolved information [25,28,32–35]. As qubit numbers are increased, however, the overhead for detection hardware and software can become limiting, motivating an exploration of complementary physics-based schemes to improve measurement fidelity in hyperfine qubits.

In this paper we borrow a detection technique widely employed in optical qubits to perform electron shelving on a hyperfine ^{171}Yb$^+$ qubit to increase detection fidelity without modification of detection hardware or software. By shelving the population of one of the qubit states to a metastable state separated by an optical transition, we can detect population remaining in the qubit manifold without being limited by off-resonant scattering and the resulting leakage to the other logical state. We implement this method using a quadrupole transition at 411 nm from the $^2S_{1/2}$ qubit manifold to the $^2D_{5/2}$ state and separately to the extremely long-lived metastable $^2F_{7/2}$ level (Fig. 1). We also employ a repump laser at 760 nm to efficiently restore all population to the qubit manifold after the detection period via the rapidly decaying $^1D[3/2]_{3/2}$ state. In our work, we further combine the shelving routine with efficient software postprocessing techniques using photons collected on an avalanche photodiode (APD) and an electron multiplying charged coupled device (EMCCD) camera, using a time-resolved, nonadaptive maximum-likelihood protocol on the APD [34] and a machine-learning-based image classifier on the EMCCD. We characterize and compare the various routines, demonstrating measurement-fidelity improvements up to 300× leveraging the $^2F_{7/2}$ level, and describe how this may be efficiently integrated into quantum information experiments.

II. TRAPPED-ION QUBIT STATE DETECTION

Various approaches are being pursued to improve qubit state detection with ions, which can be broadly classed as hardware, software, or physics based. The first category uses specialized detectors, such as superconducting nanowire single-photon detectors (SNSPDs) either stand-alone [29] or embedded in a surface-electrode rf trap [30], multichannel photomultiplier tubes (PMTs) [27,28], or fast intensified cameras [31]. Several software-based methods have been demonstrated to improve the final state estimation. Combining a record of the incident timing of photons during detection with prior knowledge such as the expected fluorescence rate and decay times τ_B and τ_D from the bright and dark states, one can infer the final state from a maximum-likelihood calculation [25]. Furthermore, if real-time data processing is available, the same detection fidelity can be achieved in shorter detection times using an adaptive version of this technique. Wölk *et al.* [34] analyzed the time-resolved detection methods for the case of ^{171}Yb$^+$, which had been experimentally demonstrated for optical qubits by Myerson *et al.* [25] and hyperfine qubits by Hume *et al.* [32] and Hemmerling *et al.* [33]. Other software-based approaches include recent work by Ding *et al.* [35] investigating the use of machine-learning methods for state estimation, implemented in hardware on a field-programmable gate array with a single ^{171}Yb$^+$ qubit; they achieved results similar to those of Seif *et al.* [28], who applied machine-learning methods to the time-resolved readout from a PMT array in postprocessing.

Detection of optical qubits falls under the physics-based approaches, achieving a very high signal-to-noise ratio through what is generally referred to as electron shelving after Dehmelt [36,37]. In such settings, measurement fidelities greater than 99.99% have been reported for an optical qubit encoded in ^{40}Ca$^+$ using time-resolved measurements of fluorescence [25] and separately, without time resolution, on an EMCCD camera [26]. The detection fidelity of an optical qubit is fundamentally limited by the lifetime of the metastable state (a T_1 decay process). Although the associated decay rate during detection is often low for typical detection times, the decay probabilities are independent for each ion and can thereby quickly become the limiting factor to the overall state-detection fidelity in larger qubit registers. To address this problem, a newer generation of fast cameras is being developed, which allow time-resolved measurements to be carried out while also providing spatial resolution for identification of the unique quantum state in a multiqubit register. First demonstrations have recently been reported for an electron-shelved readout in ^{138}Ba$^+$ [31], reaching approximately 99.99% fidelity for a single qubit and at least 99.7% in a four-qubit register.

In ^{171}Yb$^+$ the measurement-fidelity limiting factor is leakage between the hyperfine qubit levels during detection. The two logical states encoded in the $^2S_{1/2}$ levels can be distinguished by state-selective fluorescence induced by a 369 nm laser resonant with the $^2S_{1/2}\,|F=1\rangle \leftrightarrow {}^2P_{1/2}\,|F=0\rangle$ transition, which, aside from a small branching ratio to $^2D_{3/2}$, forms a closed cycling transition (Fig. 1). However, the small hyperfine splitting of 2.11 GHz between adjacent $^2P_{1/2}$ levels results in a comparatively large off-resonant scattering probability

causing leakage primarily from the bright state $^2S_{1/2}\,|F=1\rangle$ to the dark state $^2S_{1/2}\,|F=0\rangle$. The inverse occurs as well, but with a lower probability due to the effective 14.75 GHz detuning. The dynamics of this asymmetric leakage during state detection in hyperfine qubits has been analyzed theoretically by Acton *et al.* [38] and, more specifically for the case of $^{171}Yb^+$, by Wölk *et al.* [34]. A further challenge in $^{171}Yb^+$ is its low fluorescence yield compared to other isotopes without nuclear spin, such as $^{174}Yb^+$. Fluorescence increases with the strength of an applied magnetic field [39], but so does the magnetic-field sensitivity of the clock transition encoding the qubit, negatively impacting the available phase coherence time T_2.

The efficiency of a detection protocol can be quantified in two dimensions, through the measured detection error and the required detection time, both of which should be ideally minimized for practical use in quantum computing. In Fig. 2(a) we show an overview of results reported in the trapped-ion field for both hyperfine [29,30,40,41] and optical qubits [25,42] (colored open-circle markers) together with the results described in this paper (red stars, pluses, and diamonds) using the APD (solid fill) and the EMCCD (hatched fill). Figure 2(b) compares detection errors for the specific case of $^{171}Yb^+$. In Fig. 2(b), red open-circle markers represent measurements achieved without special hardware for photon collection. The green open-circle markers show $^{171}Yb^+$ detection fidelities achieved using a high-numerical-aperture (high-NA) objective [43] and the yellow open-circle marker is a measurement in $^{171}Yb^+$ using a mode-locked laser to achieve near-background-free detection in the dark periods between ultrashort pulses [44]. The blue open-circle marker uses an SNSPD to collect photons from $^{171}Yb^+$ [29]. The work we report here exceeds the results achieved with "standard" detection hardware in $^{171}Yb^+$ and if combined with high-speed optical pumping via stimulated Raman adiabatic passage (STIRAP) provides a route for field-leading performance in detection error at practically relevant measurement times. We note that while our NA (0.56) is comparable to the high-NA results from Ref. [43], the technique we introduce in this work does not depend on this special hardware and can be implemented with no changes to an existing optical setup. Indeed, we expect that lower-NA systems will see greater improvements with electron shelving as they are traditionally more susceptible to off-resonant scattering during photon collection.

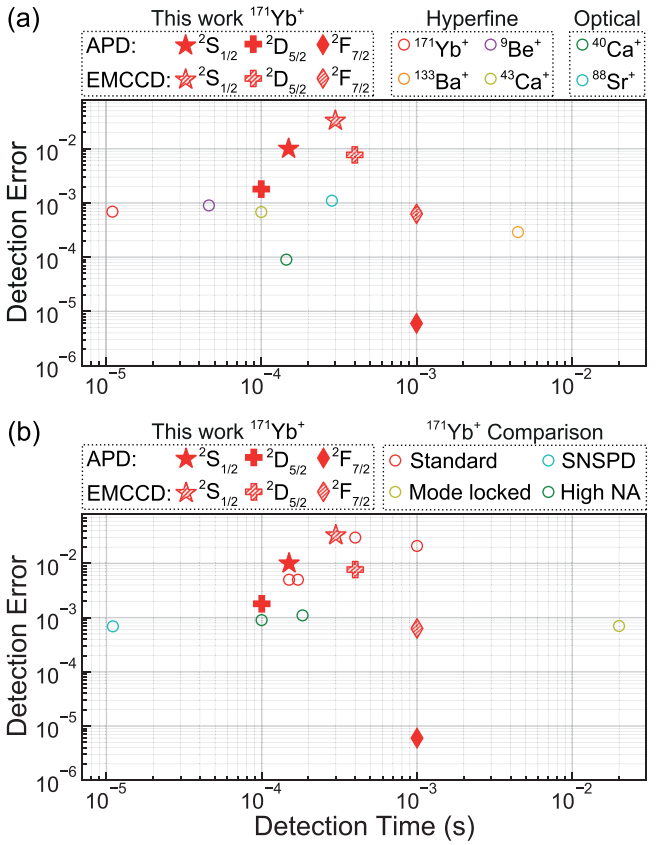

FIG. 2. Comparison of single-qubit detection errors and times for trapped-ion qubits. (a) Overview of representative results for different hyperfine qubits $^{171}Yb^+$ [29], $^{133}Ba^+$ [40], $^9Be^+$ [30], and $^{43}Ca^+$ [41], and optical qubits $^{40}Ca^+$ [25] and $^{88}Sr^+$ [42]. Red star, plus, and diamond markers represent the work presented here in $^{171}Yb^+$ using the APD (solid fill) and the EMCCD (hatched fill). Star markers indicate standard detection in the $^2S_{1/2}$ manifold and plus markers show detection after shelving to the $^2D_{5/2}$ levels. The diamond markers at 1 ms detection are achieved by detecting in the long-lived $^2F_{7/2}$ manifold in $^{171}Yb^+$. Currently, this procedure requires an additional ~100 ms for shelving, but additional laser hardware should reduce this time by two orders of magnitude using STIRAP or an active depopulation technique (see Sec. V B). (b) Comparison of results for $^{171}Yb^+$, with red circle markers representing standard detection techniques that can be straightforwardly implemented without advanced detector technology [21,28,34,35,39]. The shelving technique introduced in this work similarly requires no additional detector hardware. The remaining markers require special hardware such as a mode-locked laser [44] (yellow circle marker), superconducting nanowire single-photon detectors [29] (blue circle marker), or a high-NA objective [43] (green circle markers).

III. EXPERIMENTAL SETUP

We realize a qubit in the hyperfine clock states of $^{171}Yb^+$, designating $|0\rangle \equiv {}^2S_{1/2}\,|F=0, m_F=0\rangle$ and $|1\rangle \equiv {}^2S_{1/2}\,|F=1, m_F=0\rangle$. Our experiments are carried out in a blade-style linear Paul trap with secular trap frequencies of $\omega_{(x,y,z)}/2\pi = (1.6, 1.5, 0.5)$ MHz. The magnetic quantization field is produced by a permanent magnet, creating a 440.9(6) μT field at the ion position, which was measured using the $^2S_{1/2}$ linear Zeeman shift of 13.98(1) kHz/μT [45]. Single-qubit operations are driven with a microwave field produced by a vector signal generator[1] that is delivered through an in-vacuum loop antenna. Photons emitted during laser cooling and state detection are collected by a custom-made objective and imaged onto either an APD with an integrated detector[2] or an EMCCD[3]. The objective has a reasonably high

[1]Keysight E8267D.
[2]Laser Components COUNT-10B.
[3]Andor iXon Ultra 897.

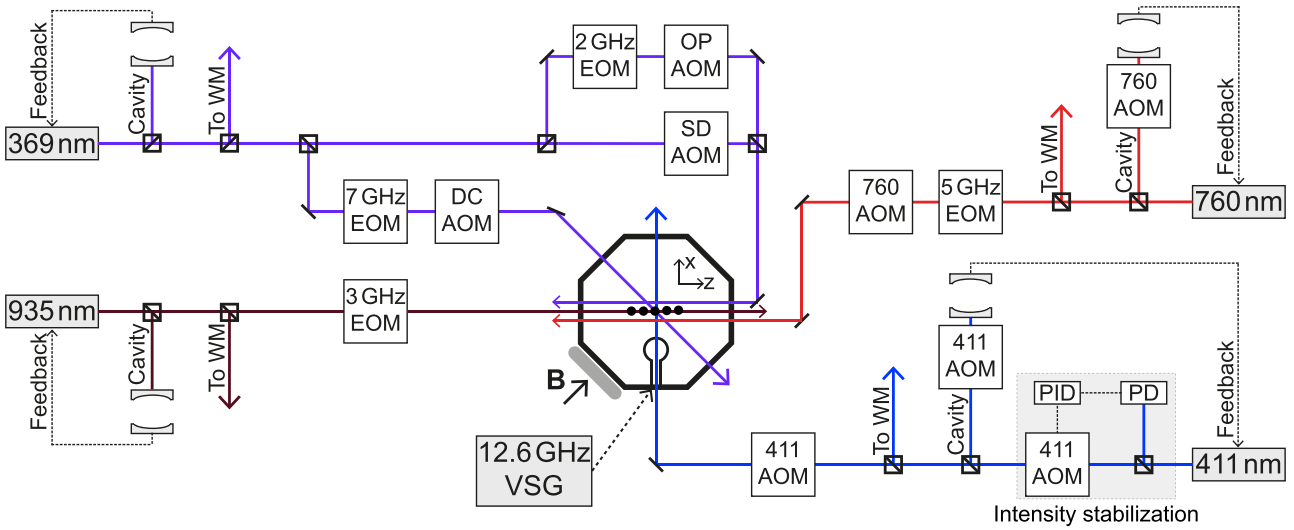

FIG. 3. Simplified overview of the laser setup and trap geometry. Beam paths for the four relevant lasers are shown, including any pertinent EOMs and AOMs, optical cavities, and the wavemeter (WM) pickoffs. The 369 nm laser is split into three beam paths for Doppler cooling (DC), optical pumping (OP), and state detection (SD). The 411 nm laser is intensity stabilized using a photodiode (PD) and a PID controller. In the center, a schematic of the vacuum chamber containing the trap is shown with five ions along the trap axis. The bottom loop in the chamber is a 12.64 GHz microwave antenna driven by a vector signal generator (VSG). The gray bar at the lower left indicates a permanent magnet creating the quantization magnetic field, **B**.

NA of 0.56 along the axis perpendicular to the weak trapping axis. This is reduced to 0.21 in the direction parallel to the weak trapping axis due to a rectangular obstruction from the trap holder. An effective NA for the resulting area is calculated to be 0.382.

A simplified energy-level diagram showing the states and transitions in $^{171}Yb^{+}$ relevant to this work is shown in Fig. 1, and a simplified schematic of the experimental setup is given in Fig. 3. Doppler cooling (DC), optical pumping (OP), and state detection (SD) utilize the $^2S_{1/2} \leftrightarrow {}^2P_{1/2}$ transition; this requires a diode laser near 369.5 nm, nominally tuned to the inner $|F = 1\rangle \leftrightarrow |F = 0\rangle$ transition that is split into three different beamlines. A second-order sideband from a 7.374 GHz electro-optic modulator (EOM) simultaneously excites the outer $|F = 0\rangle \leftrightarrow |F = 1\rangle$ transition during Doppler cooling, ensuring all manifold states are addressed. At the start of each experiment, following Doppler cooling, the ion is prepared in the qubit state $|0\rangle$ by adding a 2.105 GHz sideband via a separate EOM to the 369 nm laser; this optically pumps any population in $|1\rangle$ to $|0\rangle$ via $^2P_{1/2}\,|F = 1\rangle$ [21]. To directly measure the final qubit state, a laser at 369.5 nm light is applied to the ion without any additional modulation to selectively excite $|1\rangle$, the bright qubit state. Occasional decays from $^2P_{1/2}$ to $^2D_{3/2}$ (0.5%) remove the ion from the cooling cycle and logical state space, necessitating a repump laser at 935 nm that is operated continuously. An EOM running at 3.067 GHz adds sidebands to the 935 nm laser to ensure that both hyperfine levels of the $^2D_{3/2}$ are repumped.

In this work we introduce two additional lasers for the purpose of state detection: a 411 nm laser[4] for electron shelving from $^2S_{1/2}$ to $^2D_{5/2}$ [44,46–49] and a 760 nm laser [50–52] for repumping from the long-lived $^2F_{7/2}$ state ($\tau \approx 5.4$ years [53]) via $^1D[3/2]_{3/2}$. The 760 nm laser replaces a 638 nm laser [54] commonly used for this purpose and gives the benefit of substantially faster repumping. An EOM driven at 5.258 GHz adds sidebands to the 760 nm laser to excite both $^2F_{7/2}$ hyperfine states. The EOM frequency was experimentally calibrated by maximizing fluorescence measured on the 369 nm cooling transition when simultaneously applying the 411 nm shelving and 760 nm repumping lasers. The frequency was later updated to 5.260 GHz after measuring the center frequencies of the 760 nm repumping transitions more precisely (see Sec. IV).

We stabilize both laser frequencies through Pound-Drever-Hall locks to cylindrical Fabry-Pérot cavities[5] with a free spectral range of 1.5 GHz; the 411 nm (760 nm) cavity has a finesse of approximately 32 000 (1000–2000) and a drift rate of approximately 320 mHz/s (approximately 3.2 Hz/s). The ultralow expansion spacer of the 411 nm cavity is temperature stabilized close to the minimum of its coefficient of thermal expansion located at 38.2 °C. Absolute frequency measurements use a HeNe-calibrated wavemeter[6] with a 500 kHz precision, 10 MHz absolute accuracy at 760 nm, and 177 MHz absolute accuracy at 411 nm (due to operating more than 200 nm from the 633 nm calibration wavelength).

IV. ATOMIC SPECTROSCOPY

In order to implement electron-shelved detection using $^2D_{5/2}$ or $^2F_{7/2}$, we make use of a precision characterization of the $^2S_{1/2} \leftrightarrow {}^2D_{5/2}$ transition at 411 nm, which we report separately in [49]. Table I contains all of the relevant parameters that have been measured by our team, and we direct interested

[4]Moglabs LDL with a Moglabs Fast Servo Controller.

[5]Stable Laser Systems, Boulder CO, USA.

[6]HighFinesse WSU-10.

TABLE I. Relevant parameters for electron-shelved state detection via the $^2S_{1/2} \leftrightarrow {}^2D_{5/2}$ transition in $^{171}Yb^+$.

Parameter	This work (Expt.)
411 nm frequency for $^2S_{1/2}\,\|0,0\rangle \leftrightarrow {}^2D_{5/2}\,\|2,0\rangle$ (THz)	729.487752(177)
411 nm frequency for $^2S_{1/2}\,\|1,0\rangle \leftrightarrow {}^2D_{5/2}\,\|3,0\rangle$ (THz)	729.474917(177)
hyperfine constant of $^2D_{5/2}$ (MHz)	−63.368(1)
linear Zeeman coefficient of $^2D_{5/2}\,\|3\rangle$ (kHz/μT)	13.96(2)
linear Zeeman coefficient of $^2D_{5/2}\,\|2\rangle$ (kHz/μT)	19.61(3)
quadratic Zeeman coefficient for $^2D_{5/2}\,\|3,0\rangle$ (Hz/μT^2)	−0.350(1)
lifetime of $^2D_{5/2}\,\|3\rangle$ (ms)	7.1(4)
decay from $^2D_{5/2}\,\|3\rangle$ to $^2S_{1/2}\,\|1\rangle$	17.6(4)%
decay from $^2D_{5/2}\,\|3\rangle$ to $^2F_{7/2}$	82.4(4)%
lifetime of $^2D_{5/2}\,\|2\rangle$ (ms)	7.4(4)
decay from $^2D_{5/2}\,\|2\rangle$ to $^2S_{1/2}\,\|0\rangle$	11.1(3)%
decay from $^2D_{5/2}\,\|2\rangle$ to $^2S_{1/2}\,\|1\rangle$	7.4(3)%
decay from $^2D_{5/2}\,\|2\rangle$ to $^2F_{7/2}$	81.6(4)%
760 nm repumper center frequency (THz) after preparing $^2D_{5/2}\,\|3,0\rangle$	394.430203(16)
760 nm repumper center frequency (THz) after preparing $^2D_{5/2}\,\|2,0\rangle$	394.424943(20)

readers to Ref. [49] for full details on the measurements of the 411 nm transition, including the lifetime, branching ratios, quadratic Zeeman coefficient, and hyperfine constant of the $^2D_{5/2}$ states. From here on, we use simplified notation for the hyperfine levels in Dirac notation by omitting the F and m_F labels, shortening the labels to $|F, m_F\rangle$.

After each experiment involving the $^2D_{5/2}$ state, any population that has decayed to $^2F_{7/2}$ must be returned to the qubit manifold. There are several possible transitions over a range of wavelengths that can be driven to achieve this goal: 638 nm [55], 760 nm [50], 828 nm [54], or 864 nm [56]. Here we employ a 760 nm laser as it has been observed to have the most rapid clear-out time. This phenomenology is due to its excited energy level $^1D[3/2]_{3/2}$ exhibiting a short upper-state lifetime (29 ns [57]), and a decay path primarily to the $^2S_{1/2}$ ground states rather than other D levels [54].

In Fig. 4 we present the measured spectra for the 760 nm $^2F_{7/2} \leftrightarrow {}^1D[3/2]_{3/2}$ transition; the measurement protocol is illustrated schematically in Fig. 4(a). We first prepare the ion in one of the $^2D_{5/2}$ levels using the 411 nm shelving laser. A subsequent 10 ms wait period allows the ion to decay to either $^2S_{1/2}$ or $^2F_{7/2}$. Following the wait period, a 100 μs period of high-power on-resonance Doppler cooling induces fluorescence in cases where the ion has not decayed to $^2F_{7/2}$, and we discard these experiments in postprocessing. The 760 nm laser is then applied to clear out the $^2F_{7/2}$ state at a frequency adjusted through acousto-optic modulators (AOMs). To detect the final state, high-power on-resonance Doppler cooling light is used to determine whether the ion has returned to the $^2S_{1/2}$ manifold or remains in $^2F_{7/2}$. The probability of excitation from $^2F_{7/2}$ is plotted for states prepared in different m_F levels of $^2D_{5/2}\,|2\rangle$ [Fig. 4(b)] and $^2D_{5/2}\,|3\rangle$ [Fig. 4(c)]. The energy-level diagrams in Figs. 4(d) and 4(e) show the potentially occupied $^2F_{7/2}$ states populated through the dipole decay from $^2D_{5/2}\,|2,0\rangle$ [Fig. 4(d)] or $^2D_{5/2}\,|3,0\rangle$ [Fig. 4(e)] with the corresponding decay probabilities from the $^2D_{5/2}$ levels [46,49]. Here the 80%:3% branching ratio from $^2D_{5/2}\,|F=3\rangle$ to the different $^2F_{7/2}$ hyperfine levels is obtained from Taylor *et al.* [56]. In our current setup, we are not able to straightforwardly distinguish between population in these two hyperfine levels and hence have not measured the branching ratio in this work. We additionally indicate the possible repump pathways from $^2F_{7/2}\,|F, m_F=0\rangle$ in Figs. 4(d) and 4(e). As $^2F_{7/2} \leftrightarrow {}^1D[3/2]_{3/2}$ is an electric quadrupole (E2) coupling $\Delta m_F = 0, \pm 1, \pm 2$ transitions are possible. Consequently, given a prepared m_F level in $^2D_{5/2}$, the 760 nm peaks shown in the measurements comprise between 6 and 22 possible unresolved transitions of varying probabilities. The center frequencies of the transitions, obtained from Gaussian fits, are reported in Table I with an approximately 25× improvement in precision relative to previous results [52].

V. $^{171}Yb^+$ STATE DETECTION USING ELECTRON SHELVING

The standard detection protocol used to discriminate between the qubit states $|0\rangle$ and $|1\rangle$ in $^{171}Yb^+$ relies on detecting state-selective laser-induced fluorescence at 369 nm. Ideally, the collected photons result in two well-separated Poisson distributions corresponding to the different states. However, leakage between the qubit levels due to off-resonant excitation during detection creates one-sided tails on the photon distributions that overlap and thereby lead to detection errors.

In the following, we augment the standard detection method by prepending the measurement with pulses at 411 nm in order to transfer population from one qubit state to a metastable level. State detection is then performed using 369 nm light that drives all transitions between the $^2S_{1/2}$ and $^2P_{1/2}$ manifolds, effectively eliminating off-resonant excitations. Here the achievable detection fidelity is limited by the shelving transfer accuracy and the finite lifetime of the metastable state. As indicated in Table I, the $^2D_{5/2}$ state lifetime is approximately 7 ms, after which it decays to $^2F_{7/2}$ (∼82%) or $^2S_{1/2}$ (∼18%). This presents two possibilities for an electron-shelving-based detection protocol: (i) Transfer the population of one qubit state to $^2D_{5/2}$ and detect for duration $t \ll 7$ ms before any significant decay occurs or (ii) optically pump the $|1\rangle$ state to $^2F_{7/2}$ via $^2D_{5/2}$. In this section we describe the detection protocols using both shelving methods, discuss different software-based techniques to improve state

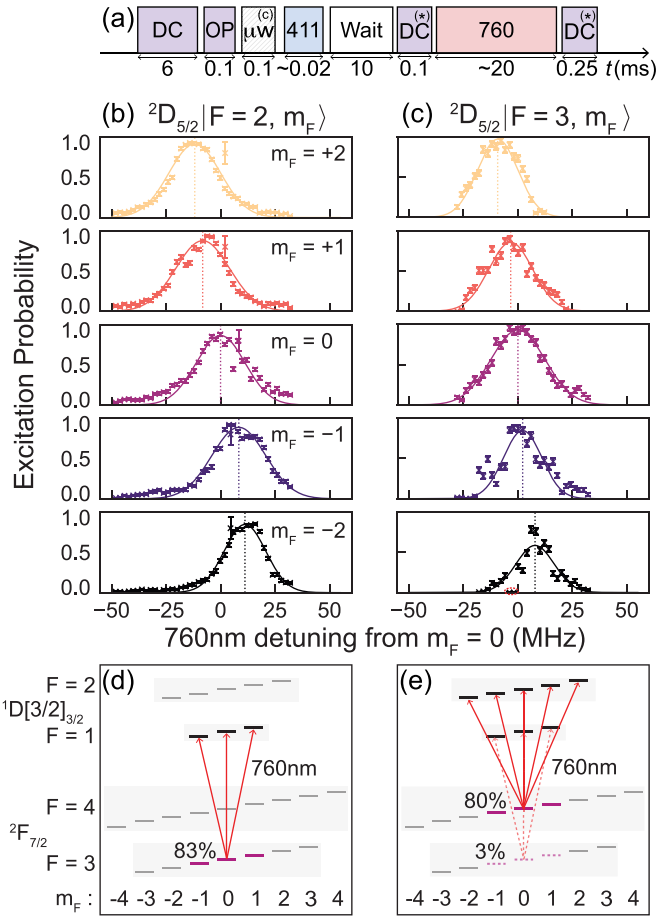

FIG. 4. Measurement of the 760 nm $^2F_{7/2}$ repump transition. (a) Schematic for the measurement protocol using the 760 nm, 411 nm, and DC and OP light at 369 nm. High-power on-resonance Doppler cooling light is utilized for detection (DC$^{(*)}$). A microwave π pulse (μw) is used in (c) to prepare $^2S_{1/2}\,|1,0\rangle$. (b) and (c) Transitions observed at 760 nm after shelving the ion to $^2D_{5/2}\,|2,m_F\rangle$ or $^2D_{5/2}\,|3,m_F\rangle$. For both transitions, the five Zeeman states $m_F = 0, \pm1, \pm2$ are individually prepared by a 411 nm pulse and the recovery probability for a given 760 nm laser frequency is shown with error bars derived from quantum projection noise. The center frequency of each excitation pathway from $^2F_{7/2}$ is extracted from a Gaussian fit. The fit for $^2D_{5/2}\,|F = 3, m_F = -2\rangle$ excludes two outlying points, which are identically zero and are indicated by the red dashed circle, where the ion is presumed to have heated. (d) and (e) Energy diagrams illustrating the possible $^2F_{7/2}$ states to which the ion can decay from $^2D_{5/2}\,|F, m_F = 0\rangle$ as well as the allowed 760 nm excitations from $^2F_{7/2}\,|F, m_F = 0\rangle$.

discrimination under these protocols, and finally compare the achieved state-detection fidelities.

A. Electron-shelved detection in $^2D_{5/2}$

The first protocol requires us to achieve an effective transfer of population from either hyperfine level in the qubit manifold to the metastable $^2D_{5/2}$ state. We begin by measuring the effectiveness of applying a π pulse on two transitions: $^2S_{1/2}\,|1\rangle \rightarrow {}^2D_{5/2}\,|3\rangle$ and $^2S_{1/2}\,|0\rangle \rightarrow {}^2D_{5/2}\,|2\rangle$ [Fig. 5(a)]. The linewidth of the 411 nm laser and the nonzero temperature of the motional modes limit the shelving efficiency associated with a single π pulse. Thus, in order to maximize population transfer, we implement a series of π pulses tuned to address multiple $^2D_{5/2}$ Zeeman levels. When shelving via $^2S_{1/2}\,|0\rangle \rightarrow {}^2D_{5/2}\,|2\rangle$, five Zeeman transitions can be driven successively, $\Delta m_F = 0, \pm1, \pm2$. By contrast, the $^2S_{1/2}\,|1\rangle \rightarrow {}^2D_{5/2}\,|3\rangle$ transition only allows three successive pulses on $\Delta m_F = 0, \pm2$ to be used, as the first-order Zeeman shift is approximately equal for the upper and lower states ($\sim$14 kHz/μT). If the $\Delta m_F = \pm1$ transitions are excited, then any population initially transferred to $^2D_{5/2}\,|3,0\rangle$ will be *deshelved* by the subsequent pulses.

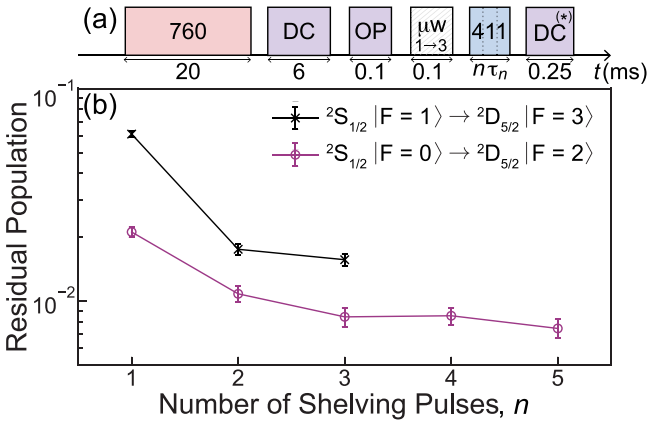

FIG. 5. Shelving efficiency of multiple π pulses. (a) Schematic showing the experimental sequence including n 411 nm shelving π pulses of length τ_n, a microwave pulse used to initialize the ion in $^2S_{1/2}\,|1,0\rangle$ before the $^2S_{1/2}\,|1\rangle \rightarrow {}^2D_{5/2}\,|3\rangle$ transition as indicated by the $1 \rightarrow 3$ label, and 369 nm light used for DC, OP, and detection. (b) Plot of the residual population in the qubit manifold $^2S_{1/2}$ after shelving via (black) $^2S_{1/2}\,|1\rangle \rightarrow {}^2D_{5/2}\,|3\rangle$ using three successive shelving pulses $\Delta m_F = \{0, +2, -2\}$ and (pink) $^2S_{1/2}\,|0\rangle \rightarrow {}^2D_{5/2}\,|2\rangle$ using five successive shelving pulses $\Delta m_F = \{0, -2, -1, +1, +2\}$. The maximum shelving fidelity is 99.3(1)% after five shelving pulses to $^2D_{5/2}\,|2\rangle$. Error bars are calculated from quantum projection noise.

The residual population in the qubit manifold after shelving is plotted in Fig. 5(b). As the number of shelving pulses is increased, the shelving fidelity improves from 93.9(2)% to 98.4(1)% for $^2S_{1/2}\,|1\rangle \rightarrow {}^2D_{5/2}\,|3\rangle$ (black) and from 97.9(2)% to 99.3(1)% for $^2S_{1/2}\,|0\rangle \rightarrow {}^2D_{5/2}\,|2\rangle$ (pink). The clock transition between the $m_F = 0$ states is driven first as its first-order magnetic-field insensitivity allows for the highest state transfer probability. In general, we observe no significant difference when changing the order of the subsequent pulses tuned to other Zeeman levels.

When using this protocol in large multiqubit registers, it is critical to ensure that the population transfer efficiency remains high for all ions throughout the experiment. Its effectiveness will be limited by laser frequency drifts and variations in coupling strength due to laser intensity or polarization gradients across the ion string. As both of these effects are often slowly varying or even static "systematic" errors, mitigation through advanced pulse sequences [58–61] can be considered in addition to regular calibration. Another commonly used routine for accurate population transfer is rapid adiabatic passage (RAP) [62–65]. This technique involves linearly

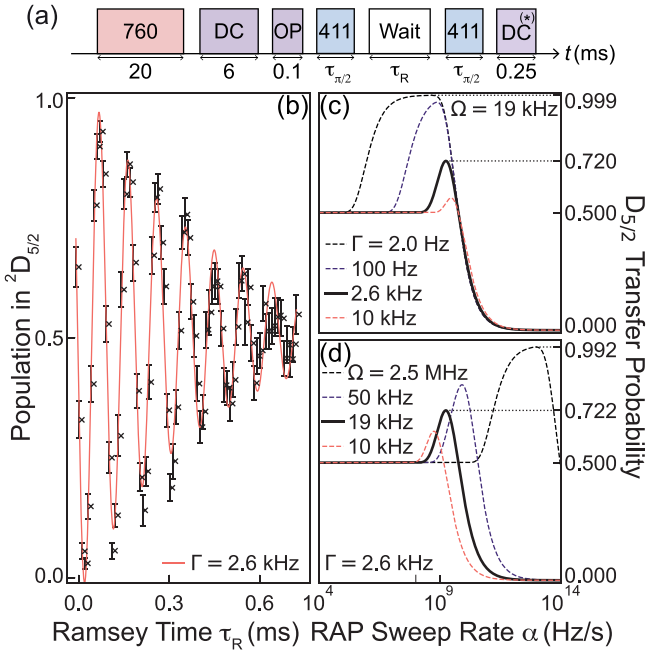

FIG. 6. Transfer fidelity using rapid adiabatic passage. (a) Protocol for Ramsey interferometry using the 411 nm laser on the $^2S_{1/2}\,|0,0\rangle \leftrightarrow {}^2D_{5/2}\,|2,0\rangle$ transition shown with a variable Ramsey wait period τ_R, the 760 nm repumping laser, two 411 nm $\pi/2$ pulses to $^2D_{5/2}$ with duration $\tau_{\pi/2}$, and the 369 nm DC, OP, and detection with high-power, resonant Doppler cooling light (DC$^{(*)}$). (b) Experimental population transferred to $^2D_{5/2}$ after the Ramsey interrogation, revealing an inverse laser coherence $\Gamma = 2.6$ kHz. (c,d) The maximum population transfer using RAP is shown for (c) fixed Rabi frequency $\Omega = 19$ kHz and varying Γ and (d) fixed $\Gamma = 2.6$ kHz and varying Ω. In both figures, the solid black line is the result of our current experimental parameters and the black dashed line shows the maximum achievable transfer.

sweeping the frequency of the shelving laser while simultaneously shaping the amplitude of the pulse to follow a Gaussian profile. The procedure is more robust to systematic errors in the pulse frequency or length than a simple π pulse, at the cost of enhanced sensitivity to high-frequency and dephasing errors [23,66,67].

In Fig. 6 we examine the theoretical maximum transfer fidelity using RAP for different inverse laser coherence times Γ and Rabi frequencies Ω. The probability of transfer using a Landau-Zener model [68] for RAP is given by

$$P_{\mathrm{LZ}} = 1 - e^{-\pi^2\Omega^2/\alpha}, \tag{1}$$

where α is the frequency sweep rate used for the RAP pulse. To incorporate the effect of a finite laser linewidth, the theory is modified to include a Markovian noise bath in a two-level dephasing model [64,69]. The transfer probability now depends on the inverse of the laser coherence Γ becoming

$$P = \tfrac{1}{2}(1 - e^{-2\pi^2\Gamma\Omega/\alpha}) + e^{-2\pi^2\Gamma\Omega/\alpha}P_{\mathrm{LZ}}, \tag{2}$$

which results in a sharp dropoff in transfer fidelity at lower sweep rates.

In our experiment we record a Rabi frequency of 19 kHz on the $^2S_{1/2}\,|0,0\rangle \rightarrow {}^2D_{5/2}\,|2,0\rangle$ clock transition and a 0.392 ms phase coherence time. This number is inferred from Ramsey interferometry shown in Figs. 6(a) and 6(b) and corresponds to an inverse coherence time of $\Gamma = 2.6$ kHz, which we attribute to the laser linewidth. The measurement protocol for the Ramsey experiment is illustrated schematically in Fig. 6(a) and the experiment data are shown in Fig. 6(b), revealing the population transferred to $^2D_{5/2}$ after the Ramsey interrogation. In Figs. 6(c) and 6(d) we plot the calculated RAP transfer fidelity against the sweep rate, as given by Eq. (2). Given our parameters $\Gamma = 2.6$ kHz and $\Omega = 19$ kHz, we could achieve a maximum transfer fidelity of 0.72 (solid black lines), which is significantly worse than the fidelity of a single π pulse ($\sim$98%). To achieve greater than 99% transfer fidelity, we would need to either improve our laser coherence to 2 Hz or increase our Rabi frequency to 2.5 MHz (black dashed lines); both of these are unfeasible in our current system. However, more reasonable parameter regimes achieving the same target can be found with two-dimensional parameter analysis, e.g., reducing the inverse coherence time to approximately 130 Hz and increasing the Rabi frequency to 100 kHz. This would be achievable using a higher laser lock bandwidth and a different laser source, respectively. We further plan to investigate numerically optimized robust control waveforms [61] to improve state transfer efficiency.

B. Electron-shelved detection in $^2F_{7/2}$

Another attractive option for electron-shelved detection in $^{171}\mathrm{Yb}^+$ uses the $^2F_{7/2}$ state with a lifetime in excess of 5 years [53], enabling longer detection periods while still eliminating off-resonant scattering. Given that $^2S_{1/2} \rightarrow {}^2F_{7/2}$ is an electric octupole transition, direct shelving to this state requires ultrastable laser systems generally only available in specialized frequency metrology laboratories [50,65,70].

To investigate this level for state detection without such a laser, we combine an "incoherent shelving" technique using the 411 nm laser and subsequent repumping at 760 nm. We optically pump the $|1\rangle$ qubit state to the $^2F_{7/2}$ manifold via $^2D_{5/2}\,|3\rangle$ using 411 nm light. As before with the electron-shelved detection in $^2D_{5/2}$, once the population has been transferred to $^2F_{7/2}$, we use high-power light resonant with the entire $^2S_{1/2}$ and $^2P_{1/2}$ manifolds to measure laser-induced fluorescence from the population remaining in the qubit manifold.

Due to the 7 ms upper state lifetime and 18% branching ratio decaying back to the qubit manifold, the incoherent shelving process requires approximately 100 ms to ensure greater than 99.9% population transfer to $^2F_{7/2}$. This timescale makes it impractical for use in quantum computing. Indeed, Ref. [71] measured an 18 ms time constant for the incoherent shelving process in $^{174}\mathrm{Yb}^+$, limited by the upper $^2D_{5/2}$ state lifetime. One way to achieve fast shelving to the F state is via a STIRAP-like scheme [72] to a state that rapidly decays to the $^2F_{7/2}$ manifold. To implement such a scheme, one could use a laser at 410 nm connecting the $^2D_{3/2}$ metastable state to the $^1[5/2]_{5/2}$ level [54,73] and combine it with light at 435 nm connecting the $^2S_{1/2}$ manifold to the $^2D_{3/2}$ state. As this scheme relies on the rapid decay of the $^1[5/2]_{5/2}$ state, it could be executed repeatedly akin to optical pumping, ensuring a high transfer efficiency to the long-lived $^2F_{7/2}$ state.

Alternatively, a pulsed two-stage scheme could be used, where multiple shelving pulses (similar to Fig. 5) are combined with active depopulation of the $^2D_{5/2}$ state via resonant light at 3.4 μm [46].

Parallel to our investigation, Ref. [71] proposed the concept of electron shelving to $^2F_{7/2}$ for the purpose of high-fidelity detection, wherein incoherent shelving to $^2F_{7/2}$ using the 411 nm laser and repumping with the 760 nm laser were demonstrated.

C. State-detection protocol comparison

In this section we compare the detection fidelity for three different detection protocols: (i) $^2S_{1/2}$ standard detection with light resonant only with the $|1\rangle$ state in the qubit manifold, (ii) $^2D_{5/2}$-shelved detection with the Doppler cooling laser tuned on resonance at high power after shelving the $|0\rangle$ qubit state to $^2D_{5/2}$ $|2\rangle$ via five successive π pulses to different Zeeman states, and (iii) $^2F_{7/2}$-shelved detection with the resonant Doppler cooling laser after incoherently shelving the $|1\rangle$ qubit state via $^2D_{5/2}$.

In all cases measurements are conducted using either an APD recording global fluorescence or an EMCCD camera providing the spatially resolved information required for experiments with multiqubit registers. Except for protocol (iii), we compare the performance of a simple threshold-based detection with a time-resolved maximum-likelihood analysis for the APD data. For all three protocols, we compare thresholding and a classifier-based software routine for analysis of EMCCD data.

The detection error is calculated by interleaving preparation of a dark and a bright qubit state and averaging the respective errors. We define the dark state error ϵ_d as the fraction of points prepared in the dark state that are recorded as bright and the bright state error ϵ_b accordingly. The overall detection error is then quantified as $\epsilon = (\epsilon_d + \epsilon_b)/2$. In order to derive a threshold value and train the image classifier, 5% of measured data are dedicated to calibration or training, with the analysis being conducted on the remaining 95% of the data.

1. APD-based detection

To find the lowest detection error achievable with the APD, we vary the length of the detection period for the three different protocols as shown in Fig. 7(a). In the simplest protocol (i) of state-dependent fluorescence detection in the qubit manifold, the photon count histograms of the bright (dark) state are described by a Poissonian distribution modified with a tail towards the dark (bright) state counts [38]. This leads to a significant overlap visible in Fig. 7(b) and correspondingly a large detection error. When one of the qubit states is shelved by five successive π pulses to $^2D_{5/2}$ $|2\rangle$ in protocol (ii), the application of detection light resonant with the entire $^2S_{1/2}$ manifold eliminates the off-resonant scattering and hence the decay tail of the bright state completely, which is shown in Fig. 7(c). A residual but suppressed tail from the dark-state distribution remains due to decays from $^2D_{5/2}$ back to the qubit manifold, with an 18% branching ratio. Finally, incoherent shelving to the long-lived $^2F_{7/2}$ state in protocol (iii) maximally suppresses the decay tails on both distributions as illustrated in Fig. 7(d). To avoid the prohibitively long

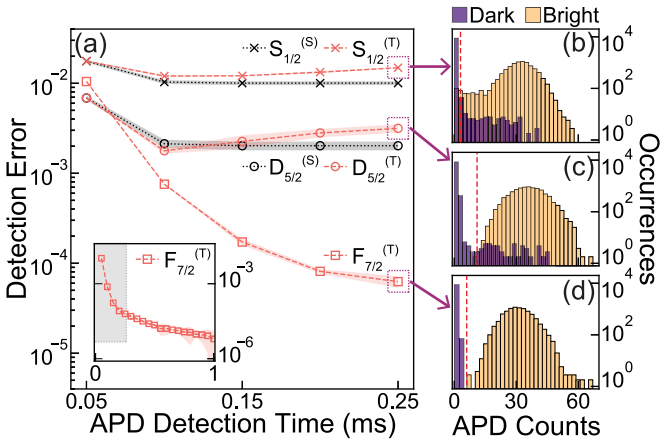

FIG. 7. APD detection for three different detection protocols and two analysis methods. (a) Detection error as a function of detection time for $^2S_{1/2}$ standard detection with thresholding (red crosses) $S_{1/2}{}^{(T)}$ and with subbinning (black crosses) $S_{1/2}{}^{(S)}$, $^2D_{5/2}$-shelved detection with thresholding (red circles) $D_{5/2}{}^{(T)}$ and with subbinning (black circles) $D_{5/2}{}^{(S)}$, and $^2F_{7/2}$-shelved detection with thresholding only (red squares) $F_{7/2}{}^{(T)}$. For both the bright and dark state measurements 20 000 points are taken when using $^2S_{1/2}$ and $^2D_{5/2}$ detection, while for $^2F_{7/2}$ we measure 1 000 000 points to resolve errors at the 1×10^{-6} level. The inset shows the extended $^2F_{7/2}$-shelved results for detection periods up to 1 ms. The gray region indicates the size of the main panel. Also shown are bright and dark state distributions with 250 μs detection time for the three methods (b) $^2S_{1/2}$, (c) $^2D_{5/2}$, and (d) $^2F_{7/2}$. The red dashed line represents the optimal threshold between the photon distributions determined from 5% of the data. Error bands in (a) show the standard deviation resulting from 20 different optimization runs to find the optimal threshold by subsampling the data.

shelving times to $^2F_{7/2}$ under optical pumping via $^2D_{5/2}$ in these measurements, rather than interleaving individual measurements of a bright and a dark ion, we interleave blocks of 1000 data points. As such, the ion is shelved only once before 1000 measurements of the dark state error are taken. The ion is then returned to the qubit manifold with the 760 nm laser in order to measure the bright state error for another 1000 points. These interleaved blocks are repeated 1000 times, yielding a total of 10^6 data points for each case. The total detection period is extended up to 1 ms for $^2F_{7/2}$-shelved detection as illustrated in the inset of Fig. 7(a).

To further improve on the detection error in the two protocols that show state decays, we also implement a maximum-likelihood estimation based on time-resolved data [34], referred to hereafter as subbinning. Here additional information about the decay dynamics during a measurement period is obtained by dividing the 250 μs overall detection period into five smaller subbins of length 50 μs. This approach improves the ability to identify decay dynamics and allows for better discrimination of dark counts originating from electronic noise or cosmic particles. For the analysis, we further require an independent measurement of average count rates and the off-resonant scattering rates for the bright and dark states. Given our standard parameters for standard $^2S_{1/2}$ detection, we measure decay times from the bright and dark states of $\tau_B \approx 2$ ms and $\tau_D \approx 30$ ms, respectively. For $^2D_{5/2}$-shelved

TABLE II. State detection errors and optimum detection times on the EMCCD and APD using three detection protocols: standard detection in $^2S_{1/2}$, electron-shelved detection in $^2D_{5/2}$, and incoherently shelved detection in $^2F_{7/2}$. These are compared for different analysis methods: basic thresholding, camera image classification, and time-resolved subbinning.

Detection \ Analysis	EMCCD thresholding		EMCCD classifier		APD thresholding		APD subbinning	
	Error	t (ms)	Error	t (ms)	Error	t (ms)	Error	t (ms)
$^2S_{1/2}$ standard	$4.3(3)\times10^{-2}$	0.3	$3.3(2)\times10^{-2}$	0.3	$1.20(6)\times10^{-2}$	0.1	$1.00(5)\times10^{-2}$	0.15
$^2D_{5/2}$-shelved	$9(1)\times10^{-3}$	0.4	$7.7(2)\times10^{-3}$	0.4	$1.8(2)\times10^{-3}$	0.1	$2.0(2)\times10^{-3}$	$\geqslant$0.15
$^2F_{7/2}$-shelved	$2(1)\times10^{-3}$	1	$6.3(3)\times10^{-4}$	1	$6(7)\times10^{-6}$	1		

detection, τ_D is given by the $\sim$7 ms upper state lifetime of the shelved state, while τ_B has an effectively infinite value. Given that there is no measurable decay during detection after shelving to $^2F_{7/2}$, we do not perform time-resolved analysis under that protocol.

2. EMCCD-based detection

To obtain spatially resolved measurements as required for multiqubit experiments, we employ an EMCCD detector. Camera-based detection requires the identification of regions of interest (ROIs) for pixel-based analyses. We locate these through Gaussian fits to the two-dimensional ion location(s) of calibration images of a bright ion(s). Further processing then happens only on ROI data extracted from the full camera images, which decreases processing time and can readily be parallelized.

As an ROI consists of multiple pixels, the thresholding method integrates their values over a certain number of "hot" pixels (corresponding to a subset of the brightest pixels) to obtain a measure of total counts in a given ROI. Alternatively, a set of calibration images obtained using ions prepared in the dark and bright states can be used to train a random forest classifier [74] for each ROI in order to identify $|0\rangle$ and $|1\rangle$. If trained on reliable data, this method is expected to be superior to the simple thresholding model, as it will consider not just the net fluorescence in the region of interest but also *correlations* between the counts on different pixels.

We compare the two spatial analysis methods across the three different detection protocols: standard $^2S_{1/2}$, $^2D_{5/2}$-shelved, and $^2F_{7/2}$-shelved. In Fig. 8(a) we evaluate the measured detection error as a function of detection time for the first two protocols. The $^2S_{1/2}$ standard detection (cross markers) is compared to the $^2D_{5/2}$-shelved detection (open circles) and each data set is analyzed using the thresholding method (red) and the image classifier (black). These data clearly show that the shelved detection is superior to standard and that the image classifier can yield appreciable improvements under short to intermediate detection times. This is likely related to the larger number of mislabeled training images due to state decays, potentially offering room for further improvement.

The change in detection error at different detection times can be understood by examining the bright and dark histograms for $^2D_{5/2}$-shelved detection [Figs. 8(b)–8(d)]. At short detection times, the distributions have a large overlap, with electrical noise in the camera dominating the signal [Fig. 8(b), 0.05 ms detection period]. At long detection periods [Fig. 8(d), 1.5 ms], the bright distribution mean has increased sufficiently to separate it from the dark distribution, but state decays become dominant due to the 7 ms lifetime of $^2D_{5/2}$ producing a decay tail from the dark distribution. At the optimum detection period, these two error contributions are balanced [Fig. 8(c), 0.4 ms detection period].

D. Summary of results

We summarize our findings of the lowest measured errors for all detection protocols and analysis methods in Table II.

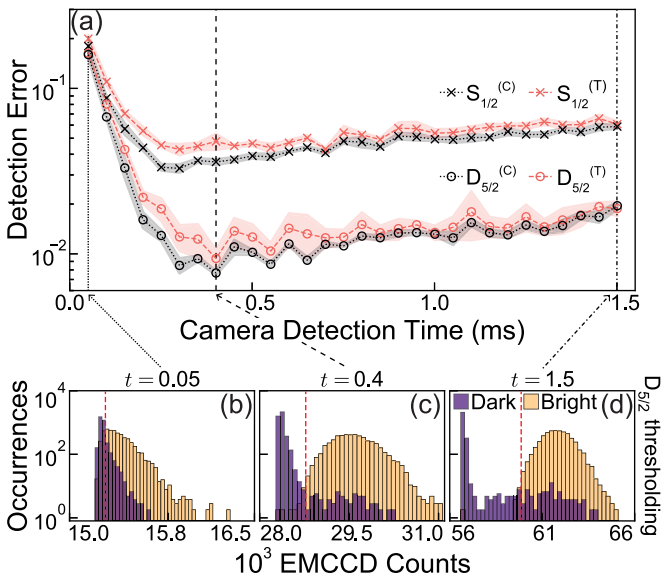

FIG. 8. EMCCD-based detection for two different detection protocols and analysis methods. (a) Detection error using $^2S_{1/2}$ standard detection with thresholding (red crosses) $S_{1/2}{}^{(T)}$ and the image classifier (black crosses) $S_{1/2}{}^{(C)}$ and electron-shelved detection after quintuple shelving to $^2D_{5/2}$ $|2\rangle$ with thresholding (red circles) $D_{5/2}{}^{(T)}$ and the classifier (black circles) $D_{5/2}{}^{(C)}$. The lines show the means after sampling five different sets of training data and shaded bands are $\pm1\sigma$. Five thousand measurements are taken at each point for both the bright and dark prepared states. Five percent of the total data set is employed for training and used for identification of hot pixels, thresholds, and classifier training. (b)–(d) Camera histograms for $^2D_{5/2}$-shelved detection at three detection times, illustrating how an optimum time is found for thresholding. For each histogram, the dashed red line marks the optimal threshold between dark and bright.

Overall, we achieve a 5.6× improvement in fidelity using electron-shelved detection in $^2D_{5/2}$ compared to standard $^2S_{1/2}$ detection, measuring an error of $1.8(2) \times 10^{-3}$ with a 100 μs detection time on the APD. When using the EMCCD, we record a minimum error of $7.7(2) \times 10^{-3}$ using $^2D_{5/2}$-shelved detection, 4.3× lower than the best observed error using standard detection. For $^2F_{7/2}$-shelved detection with a 1 ms detection time, the detection error is reduced by another factor of 300× (12×) to $6(7) \times 10^{-6}$ [$6.3(3) \times 10^{-4}$] on the APD (EMCCD).

VI. CONCLUSION

In this work we have demonstrated that it is possible to combine the benefits of a long-lived, first-order magnetic-field insensitive hyperfine qubit with the high-fidelity detection typically observed in an optical qubit. By first shelving the population in one qubit state of $^{171}Yb^+$ to a metastable level, we are able to use high-power near-resonant Doppler cooling light to perform efficient state discrimination without suffering off-resonant leakage. To enable scaling to larger qubit registers, we also characterize the detection error after shelving to $^2D_{5/2}$ when using a spatially resolving EMCCD. For both the APD and EMCCD detectors we compare the performance of software routines for processing photon detection data. This involves either analyzing time-resolved information about the incoming photons collected on the APD or exploiting spatial correlations between EMCCD pixels using a classifier routine.

We also validate that the state-detection error in our system can be further reduced by shelving to the long-lived $^2F_{7/2}$ manifold. The laser systems used in one of two schemes we outline could be used to overcome the prohibitively long optical pumping time to $^2F_{7/2}$, making this a viable avenue for ultrahigh-fidelity detection.

Ultimately our results foreshadow the possibility of combining novel data-processing software routines with physics-based techniques in the future to further reduce measurement errors without requiring extensive hardware modifications. When combined with an efficient repump laser at 760 nm to reset the qubit state, we believe the electron-shelving-based detection routine presented here will improve the practicality and scalability of current $^{171}Yb^+$ quantum devices.

Note added. Recently, we became aware of independent work at UCLA investigating shelving to the $^2F_{7/2}$ manifold for high-fidelity detection, as in Ref. [71].

ACKNOWLEDGMENTS

This work was partially supported by the Intelligence Advanced Research Projects Activity Grant No. W911NF-16-1-0070, the U.S. Army Research Office Grant No. W911NF-14-1-0682, the Australian Research Council Centre of Excellence for Engineered Quantum Systems Grant No. CE170100009, and a private grant from H. Harley and A. Harley.

[1] T. P. Harty, D. T. C. Allcock, C. J. Ballance, L. Guidoni, H. A. Janacek, N. M. Linke, D. N. Stacey, and D. M. Lucas, Phys. Rev. Lett. **113**, 220501 (2014).

[2] M. A. Sepiol, A. C. Hughes, J. E. Tarlton, D. P. Nadlinger, T. G. Ballance, C. J. Ballance, T. P. Harty, A. M. Steane, J. F. Goodwin, and D. M. Lucas, Phys. Rev. Lett. **123**, 110503 (2019).

[3] J. P. Gaebler, T. R. Tan, Y. Lin, Y. Wan, R. Bowler, A. C. Keith, S. Glancy, K. Coakley, E. Knill, D. Leibfried, and D. J. Wineland, Phys. Rev. Lett. **117**, 060505 (2016).

[4] C. J. Ballance, T. P. Harty, N. M. Linke, M. A. Sepiol, and D. M. Lucas, Phys. Rev. Lett. **117**, 060504 (2016).

[5] T. Choi, S. Debnath, T. A. Manning, C. Figgatt, Z.-X. Gong, L.-M. Duan, and C. Monroe, Phys. Rev. Lett. **112**, 190502 (2014).

[6] P. H. Leung, K. A. Landsman, C. Figgatt, N. M. Linke, C. Monroe, and K. R. Brown, Phys. Rev. Lett. **120**, 020501 (2018).

[7] A. R. Milne, C. L. Edmunds, C. Hempel, F. Roy, S. Mavadia, and M. J. Biercuk, Phys. Rev. Appl. **13**, 024022 (2020).

[8] V. M. Schäfer, C. J. Ballance, K. Thirumalai, L. J. Stephenson, T. G. Ballance, A. M. Steane, and D. M. Lucas, Nature (London) **555**, 75 (2018).

[9] C. Zhang, F. Pokorny, W. Li, G. Higgins, A. Pöschl, I. Lesanovsky, and M. Hennrich, Nature (London) **580**, 345 (2020).

[10] K. Wright *et al.*, Nat. Commun. **10**, 5464 (2019).

[11] C. D. B. Bentley, H. Ball, M. J. Biercuk, A. R. R. Carvalho, M. R. Hush, and H. J. Slatyer, Adv. Quantum Technol. **3**, 2000044 (2020).

[12] Y. Nam *et al.*, npj Quantum Inf. **6**, 33 (2020).

[13] A. Erhard, H. P. Nautrup, M. Meth, L. Postler, R. Stricker, M. Stadler, V. Negnevitsky, M. Ringbauer, P. Schindler, H. J. Briegel, R. Blatt, N. Friis, and T. Monz, Nature (London) **589**, 220 (2021).

[14] L. Egan, D. M. Debroy, C. Noel, A. Risinger, D. Zhu, D. Biswas, M. Newman, M. Li, K. R. Brown, M. Cetina, and C. Monroe, arXiv:2009.11482.

[15] P. Schindler, J. T. Barreiro, T. Monz, V. Nebendahl, D. Nigg, M. Chwalla, M. Hennrich, and R. Blatt, Science **332**, 1059 (2011).

[16] D. Nigg, M. Müller, E. A. Martinez, P. Schindler, M. Hennrich, T. Monz, M. A. Martin-Delgado, and R. Blatt, Science **345**, 302 (2014).

[17] A. Bermudez *et al.*, Phys. Rev. X **7**, 041061 (2017).

[18] C. D. Bruzewicz, J. Chiaverini, R. McConnell, and J. M. Sage, Appl. Phys. Rev. **6**, 021314 (2019).

[19] J. Benhelm, G. Kirchmair, C. F. Roos, and R. Blatt, Phys. Rev. A **77**, 062306 (2008).

[20] G. Kirchmair, J. Benhelm, F. Zähringer, R. Gerritsma, C. F. Roos, and R. Blatt, Phys. Rev. A **79**, 020304(R) (2009).

[21] S. Olmschenk, K. C. Younge, D. L. Moehring, D. N. Matsukevich, P. Maunz, and C. Monroe, Phys. Rev. A **76**, 052314 (2007).

[22] H. Ball, W. D. Oliver, and M. J. Biercuk, npj Quantum Inf. **2**, 16033 (2016).

[23] C. L. Edmunds, C. Hempel, R. J. Harris, V. Frey, T. M. Stace, and M. J. Biercuk, Phys. Rev. Research **2**, 013156 (2020).

[24] D. J. Wineland, J. C. Bergquist, J. J. Bollinger, and W. M. Itano, Phys. Scripta **1995**, 286 (1995).

[25] A. H. Myerson, D. J. Szwer, S. C. Webster, D. T. C. Allcock, M. J. Curtis, G. Imreh, J. A. Sherman, D. N. Stacey, A. M. Steane, and D. M. Lucas, Phys. Rev. Lett. **100**, 200502 (2008).

[26] A. H. Burrell, D. J. Szwer, S. C. Webster, and D. M. Lucas, Phys. Rev. A **81**, 040302(R) (2010).

[27] S. Debnath, N. M. Linke, C. Figgatt, K. A. Landsman, K. Wright, and C. Monroe, Nature (London) **536**, 63 (2016).

[28] A. Seif, K. A. Landsman, N. M. Linke, C. Figgatt, C. Monroe, and M. Hafezi, J. Phys. B **51**, 174006 (2018).

[29] S. Crain, C. Cahall, G. Vrijsen, E. E. Wollman, M. D. Shaw, V. B. Verma, S. W. Nam, and J. Kim, Commun. Phys. **2**, 97 (2019).

[30] S. L. Todaro, V. B. Verma, K. C. McCormick, D. T. C. Allcock, R. P. Mirin, D. J. Wineland, S. W. Nam, A. C. Wilson, D. Leibfried, and D. H. Slichter, Phys. Rev. Lett. **126**, 010501 (2021).

[31] L. A. Zhukas, P. Svihra, A. Nomerotski, and B. B. Blinov, Phys. Rev. A **103**, 062614 (2021).

[32] D. B. Hume, T. Rosenband, and D. J. Wineland, Phys. Rev. Lett. **99**, 120502 (2007).

[33] B. Hemmerling, F. Gebert, Y. Wan, and P. O. Schmidt, New J. Phys. **14**, 023043 (2012).

[34] S. Wölk, C. Piltz, T. Sriarunothai, and C. Wunderlich, J. Phys. B **48**, 075101 (2015).

[35] Z.-H. Ding, J.-M. Cui, Y.-F. Huang, C.-F. Li, T. Tu, and G.-C. Guo, Phys. Rev. Appl. **12**, 014038 (2019).

[36] H. Dehmelt, Bull. Am. Phys. Soc. **20**, 60 (1975).

[37] W. Nagourney, J. Sandberg, and H. Dehmelt, Phys. Rev. Lett. **56**, 2797 (1986).

[38] M. Acton, K. A. Brickman, P. C. Haljan, P. J. Lee, L. Deslauriers, and C. Monroe, Quantum Inf. Comput. **6**, 465 (2005).

[39] S. Ejtemaee, R. Thomas, and P. C. Haljan, Phys. Rev. A **82**, 063419 (2010).

[40] J. E. Christensen, D. Hucul, W. C. Campbell, and E. R. Hudson, npj Quantum Inf. **6**, 35 (2020).

[41] T. P. Harty, High-Fidelity microwave-driven quantum logic in intermediate-field $^{43}Ca^{+}$, Ph.D. thesis, University of Oxford, 2013.

[42] A. Keselman, Y. Glickman, N. Akerman, S. Kotler, and R. Ozeri, New J. Phys. **13**, 073027 (2011).

[43] R. Noek, G. Vrijsen, D. Gaultney, E. Mount, T. Kim, P. Maunz, and J. Kim, Opt. Lett. **38**, 4735 (2013).

[44] C. Roman, A. Ransford, M. Ip, and W. C. Campbell, New J. Phys. **22**, 073038 (2020).

[45] W. F. Meggers, J. Res. NBS A: Phys. Chem. **71**, 396 (1967).

[46] M. Roberts, P. Taylor, S. V. Gateva-Kostova, R. B. M. Clarke, W. R. C. Rowley, and P. Gill, Phys. Rev. A **60**, 2867 (1999).

[47] J. Keller, Spectroscopic characterization of ion motion for an optical clock based on coulomb crystals, Ph.D. thesis, University of Hannover, 2015.

[48] T. Feldker, H. Fürst, H. Hirzler, N. V. Ewald, M. Mazzanti, D. Wiater, M. Tomza, and R. Gerritsma, Nat. Phys. **16**, 413 (2020).

[49] T. Tan, C. L. Edmunds, A. R. Milne, M. J. Biercuk, and C. Hempel, Precision characterization of the $D_{5/2}$ state and quadratic Zeeman coefficient in $^{171}Yb^{+}$, arXiv:2012.14187.

[50] N. Huntemann, M. Okhapkin, B. Lipphardt, S. Weyers, C. Tamm, and E. Peik, Phys. Rev. Lett. **108**, 090801 (2012).

[51] Y.-Y. Jau, J. D. Hunker, and P. D. D. Schwindt, AIP Adv. **5**, 117209 (2015).

[52] S. Mulholland, H. A. Klein, G. P. Barwood, S. Donnellan, P. B. R. Nisbet-Jones, G. Huang, G. Walsh, P. E. G. Baird, and P. Gill, Rev. Sci. Instrum. **90**, 033105 (2019).

[53] M. Roberts, P. Taylor, G. P. Barwood, W. R. C. Rowley, and P. Gill, Phys. Rev. A **62**, 020501(R) (2000).

[54] K. Sugiyama, Jpn. J. Appl. Phys. **38**, 2141 (1999).

[55] P. Gill, H. A. Klein, A. P. Levick, M. Roberts, W. R. C. Rowley, and P. Taylor, Phys. Rev. A **52**, R909 (1995).

[56] P. Taylor, M. Roberts, S. V. Gateva-Kostova, R. B. M. Clarke, G. P. Barwood, W. R. C. Rowley, and P. Gill, Phys. Rev. A **56**, 2699 (1997).

[57] R. W. Berends, E. H. Pinnington, B. Guo, and Q. Ji, J. Phys. B **26**, L701 (1993).

[58] R. Tycko, Phys. Rev. Lett. **51**, 775 (1983).

[59] M. H. Levitt, Prog. Nucl. Mag. Res. Sp. **18**, 61 (1986).

[60] C. Kabytayev, T. J. Green, K. Khodjasteh, M. J. Biercuk, L. Viola, and K. R. Brown, Phys. Rev. A **90**, 012316 (2014).

[61] H. Ball, M. J. Biercuk, A. Carvalho, J. Chen, M. Hush, L. A. D. Castro, L. Li, P. J. Liebermann, H. J. Slatyer, C. Edmunds, V. Frey, C. Hempel, and A. Milne, Quantum Sci. Technol., doi: 10.1088/2058-9565/abdca6.

[62] N. V. Vitanov, T. Halfmann, B. W. Shore, and K. Bergmann, Annu. Rev. Phys. Chem. **52**, 763 (2001).

[63] C. Wunderlich, T. Hannemann, T. Körber, H. Häffner, C. Roos, W. Hänsel, R. Blatt, and F. Schmidt-Kaler, J. Mod. Opt. **54**, 1541 (2007).

[64] T. Noel, M. R. Dietrich, N. Kurz, G. Shu, J. Wright, and B. B. Blinov, Phys. Rev. A **85**, 023401 (2012).

[65] H. A. Fürst, C.-H. Yeh, D. Kalincev, A. P. Kulosa, L. S. Dreissen, R. Lange, E. Benkler, N. Huntemann, E. Peik, and T. E. Mehlstäubler, Phys. Rev. Lett. **125**, 163001 (2020).

[66] X.-J. Lu, X. Chen, A. Ruschhaupt, D. Alonso, S. Guérin, and J. G. Muga, Phys. Rev. A **88**, 033406 (2013).

[67] A. Soare, H. Ball, D. Hayes, J. Sastrawan, M. C. Jarratt, J. J. McLoughlin, X. Zhen, T. J. Green, and M. J. Biercuk, Nat. Phys. **10**, 825 (2014).

[68] C. Zener, Proc. R. Soc. London Ser. A **137**, 696 (1932).

[69] X. Lacour, S. Guérin, L. P. Yatsenko, N. V. Vitanov, and H. R. Jauslin, Phys. Rev. A **75**, 033417 (2007).

[70] N. Huntemann, B. Lipphardt, M. Okhapkin, C. Tamm, E. Peik, A. V. Taichenachev, and V. I. Yudin, Phys. Rev. Lett. **109**, 213002 (2012).

[71] A. M. Ransford, Old Dog, new trick: high fidelity, background-free state detection of an ytterbium ion qubit, Ph.D. thesis, University of California, Los Angeles, 2020, available at https://escholarship.org/content/qt0w24t8kr/qt0w24t8kr.pdf.

[72] N. V. Vitanov, A. A. Rangelov, B. W. Shore, and K. Bergmann, Rev. Mod. Phys. **89**, 015006 (2017).

[73] M. Schacht, J. R. Danielson, S. Rahaman, J. R. Torgerson, J. Zhang, and M. M. Schauer, J. Phys. B **48**, 065003 (2015).

[74] F. Pedregosa *et al.*, J. Mach. Learn Res. **12**, 2825 (2011).